HANSER

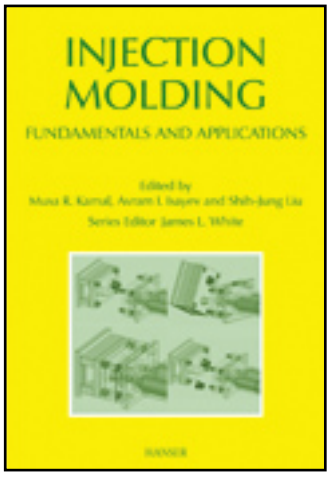

Sample Pages

Injection Molding

Technology and Fundamentals

Herausgegeben von Musa R. Kamal, Avram I. Isayev

ISBN: 978-3-446-41685-7

For further information and order see

http://www.hanser.de/978-3-446-41685-7
or contact your bookseller.

3.5.5.2 Equation of State

The equation of state gives a dependence of the interfacial tension on the surfactant concentration. One of the most popular equation of state is the Langmuir adsorption isotherm, the so called Szyszkowski equation (often called Langmuir equation of state)

$$\sigma(\Gamma) = \sigma_0 + R\,T \ln(1 - \Gamma/\Gamma_\infty) \tag{3.100}$$

where Γ_∞ is the maximum concentration for complete surface coverage in a monomolecular film, and $R\,T$ is the product of the gas constant and the temperature. This equation has the advantage to be valid also for large surfactant concentrations in contrast to the linear equation of state.

In dimensionless terms, Eq. (3.98) becomes

$$\sigma(\Gamma) = \frac{1 + E \ln(1 - x\,\Gamma)}{1 + E \ln(1 - x)} \tag{3.101}$$

where $E = R\,T/\sigma_0$ is the elasticity number and $x = \Gamma_{eq}/\Gamma_\infty$ is the surface coverage. With this definition of the elasticity number (based on σ_0 rather than σ_{eq}), E does not depend on the surfactant coverage x. More complicated equations of state have also been used, for example the Frumkin isotherm or two-phase equation of state. Their disadvantage, however, is a larger number of parameters.

3.5.5.3 Drop Shapes

The presence of surfactants can significantly alter the drop deformation and consequently the value of the critical capillary number. Surfactants lower the interfacial tension and, in general, promote drop deformation. When the drop is subjected to an external flow, the surfactant concentration becomes nonuniform due to the surfactant convection, introducing interfacial tension gradients, known as Marangoni stress. The Marangoni stress effects the drop deformation and the external flow as well (compare the pattern of the external flow for both frames in Fig. 3.111 (right)). Figures 3.111–3.117 show some results obtained by a boundary integral formulation. In addition, the internal circulation in the drop phase, see Fig. 3.111 (left), also contributes to the surfactant distribution, which differs significantly from that in extensional flows.

3.5.5.4 Modes of Drop Breakage

An important question regarding the drop-size distribution in a suspension is: At what conditions drops will remain compact and when they will break up? In the case of a drop with constant interfacial tension, the answer was already given by the dependence $\mathrm{Ca}_{cr}(\lambda)$, see also Fig. 3.88. The presence of surfactants can significantly alter drop deformation and breakup and, consequently, the critical capillary number. The influence of the surface coverage on the critical capillary number is shown in Fig. 3.112. It is seen that for small λ, the presence

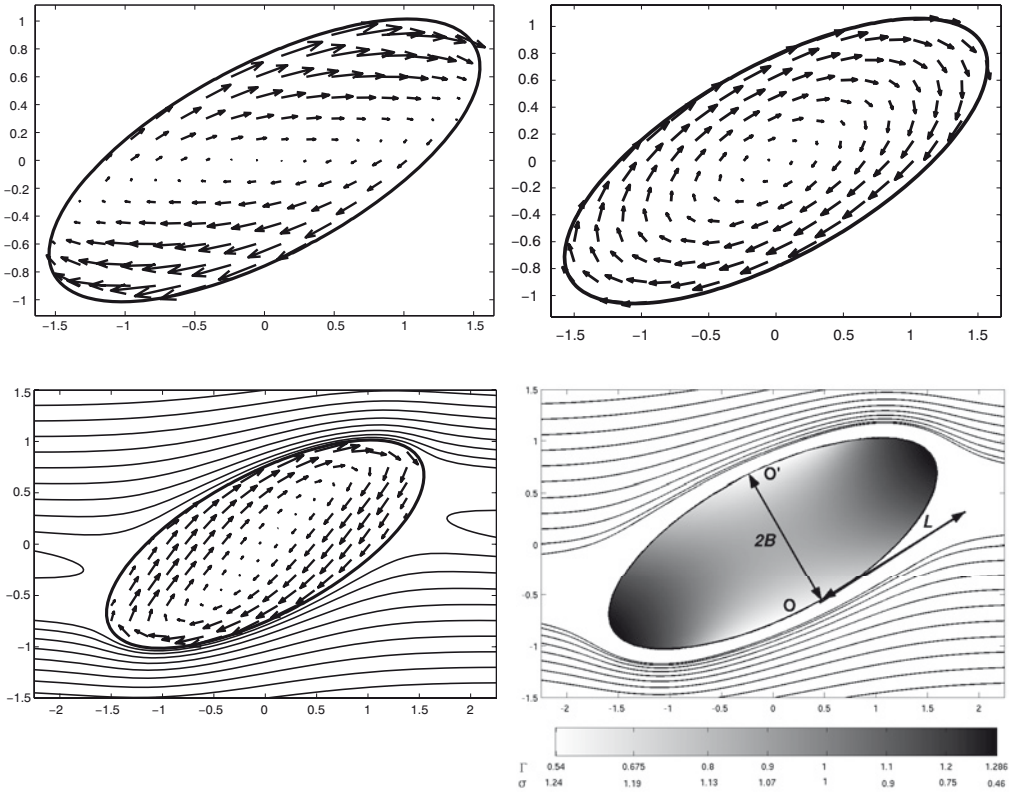

Figure 3.111: The interfacial velocity for $\lambda = 0.1$ at: (top left) $x = 0$ (no surfactant), Ca = 0.4; (bottom left) $x = 0.975$, Ca = 0.525. Streamlines, velocity, and surfactant concentration for steady drop shapes at $\lambda = 0.1$: (top right) no surfactant at Ca = 0.4; (bottom right) surfactant at $E = 0.2$, $x = 0.75$ and Ca = 0.265. In both cases, the deformation is about $D = (L - B)/(L + B) = 0.43$ (the streamlines at the same levels and the velocity field are shown in the *x*-*y* plane) [90]

of surfactants on the drop interface leads to a decrease of Ca_{cr} due to the tip-streaming. This is the case even for an extremely small surface coverage; note that at $x = 0.1$ the decrease of interfacial tension is only approx. 2%, $\sigma_0/\sigma_{eq} = 1.02$.

The previously discussed effect of independence of drop deformation on viscosity ratio at small λ is expressed here as a plateau part of $Ca_{cr}(\lambda)$ for all values of x considered. The height of the plateau has a similar dependence on surface coverage as drop deformation: with increasing surface coverage the critical capillary number initially decreases, until $x = 0.75$, after which it increases (see the inset in Fig. 3.112). This behavior agrees well with previous results for axisymmetric and planar extensional flows. Figure 3.112 and also Fig. 3.113 indicate that for $\lambda \leq 0.1$, tip-streaming appears for $0.1 < x \leq 0.95$, which in terms of the relative interfacial tension is $1.02 < \sigma_0/\sigma_{eq} < 2.5$.

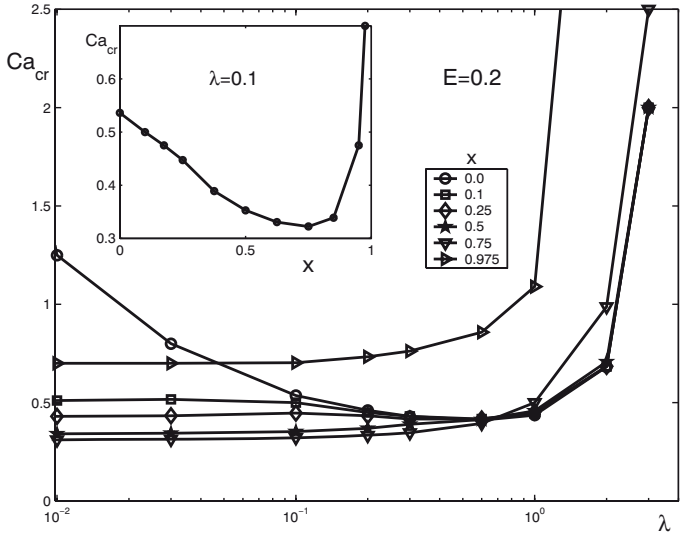

Figure 3.112: The critical capillary number as a function of the viscosity ratio for different surfactant coverage [90]

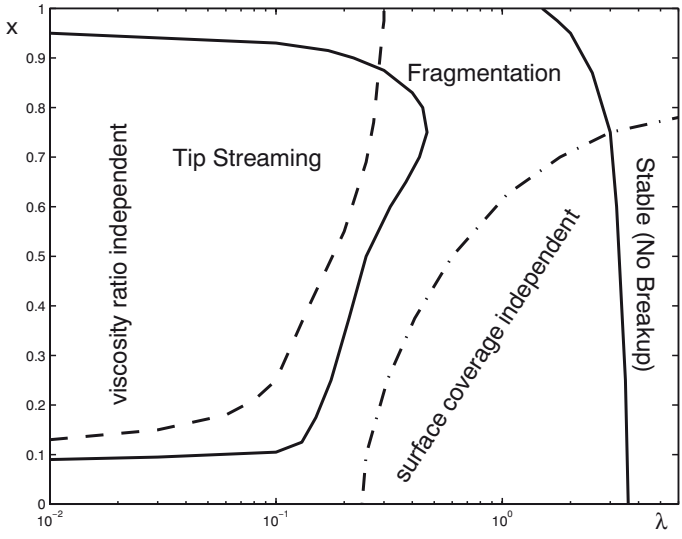

Figure 3.113: Phase diagram: Surfactant coverage x versus viscosity ratio λ.
The solid lines bound to the different regions of drop breakup (fragmentation or tip-streaming/dropping). The boundaries of surfactant dominated (viscosity ratio has no influence) and drop viscosity dominated (surface coverage has no influence) regions are given by the dashed and dash-dotted lines, respectively [90]

The regions where drop deformation is independent of the viscosity ratio (dashed line) or surface coverage (dash-dotted line) are also shown in Fig. 3.113. The application of the present results is limited to the case of initially spherical drops subjected to a homogeneous shear flow with slowly increased shear rate. As in the case of pure interfaces, the critical conditions for drop breakup can depend on the initial drop shape and/or nonhomogeneous shear flow.

Figure 3.114 shows a typical drop shape at the moment when the daughter drop is emitted. Also, a picture of the boundary integral mesh is shown, which already indicates the difficulties faced when solving these types of problems computationally. The process of tip stretching and daughter drop formation is shown in Fig. 3.115. With increasing capillary number, the surfactant concentration at the drop tips increases and consequently the interfacial tension decreases. When Ca exceeds the critical value, Ca_{cr}, the interfacial forces at the tips become almost zero, Fig. 3.115 (top), and can no longer resist the viscous deformation forces. Thus, the tip is stretched further, Fig. 3.115 (middle). With progressing stretching, however, the interfacial area increases and the surfactant is locally diluted, leading to an increase of the interfacial tension, Fig. 3.115 (bottom). This promotes capillary breakup of tiny drops, about 25 times smaller than the main drop. The equivalent surfactant concentration of the daughter drop is about 97% of the saturation limit with an equivalent interfacial tension about 1/3 of that of the main drop. This is in good qualitative agreement with the experimental observation in simple shear flow, as well as with the simulations of Eggleton *et al.* [153].

The dependence of the thread and daughter drop size on the capillary number shows that the size of the daughter drop increases with increasing Ca, referring to 'tip-dropping'. Figure 3.116 shows that at larger capillary numbers, the main drop undergoes a larger deformation. The zoomed tip region, presented in Fig. 3.117, indicates that the size of the daughter drop increases with Ca. The thread size initially, for values $0.4 \leq Ca \leq 0.5$, increases and is

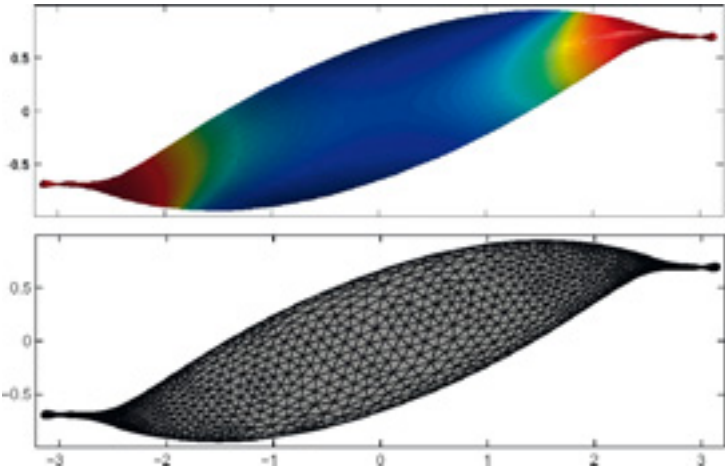

Figure 3.114: Tip streaming at $E = 0.2$, $x = 0.5$, $\lambda = 0.1$ and Ca = 0.38. The critical capillary number is about $Ca_{cr} = 0.353$

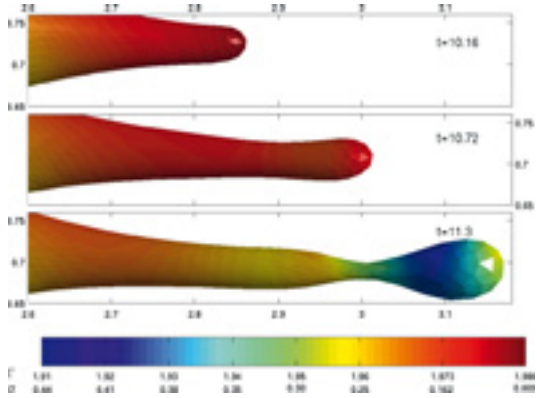

Figure 3.115: The evolution of the tip for the case shown in Fig. 3.114 [90]

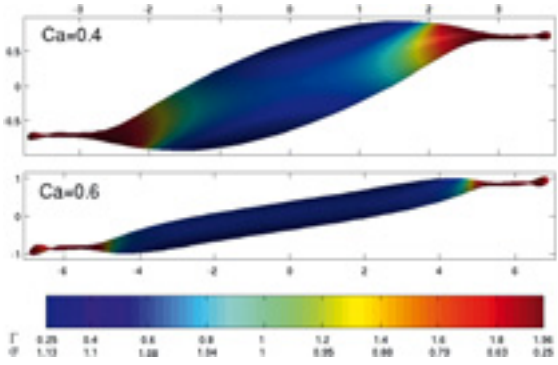

Figure 3.116: Tip dropping at $E = 0.2$, $x = 0.5$, $\lambda = 0.1$: Ca = 0.4 (top); Ca = 0.6 (bottom) [90]

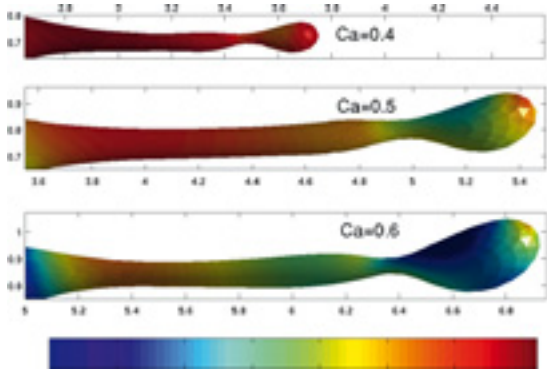

Figure 3.117: The zoomed tip region for three different capillary numbers. The frames show the tip regions just before dropping. The first and the third frames correspond to Fig. 3.116 (all three frames are scaled equally) [90]

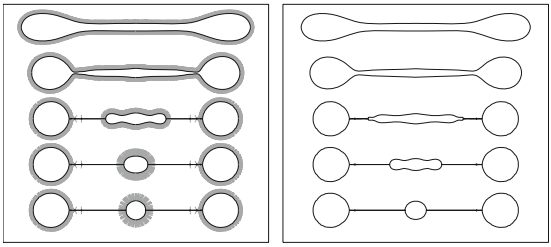

Figure 3.118: Breakup of a drop elongated at Ca = 0.1 to $L_0 = 5$. Left with surfactant ($\beta = 0.5$, Pe = 0), right without. Lines perpendicular to interface indicate surfactant concentration. In daughter drops in centre: $\sigma = 0.89\,\sigma_{ref}$, while for outer drops: $\sigma = 1.42\,\sigma_{ref}$ [91]

then almost unaffected by a further increase of Ca. The equivalent interfacial tension of the daughter drop also increases with Ca from approx. $\sigma_{eq} = 0.4$ at Ca = 0.4 to almost twice this value at Ca = 0.6.

Also interesting is to investigate the influence of surfactants in symmetric breakups after extension by extensional flow. Figure 3.118 shows on the left hand side the surfactant concentration during breakup, indicated by the size of the bars perpendicular to the surface, compared to breakup of a clean surface on the right. Where breakup is hardly influenced by the presence of surfactants, nor are the size and number of resulting drops, those drops themselves are quite different, since they collect different amounts of surfactants, thus will have a rather large change in surface tension.

Figures 3.119 and 3.120 show that the size of the surfactant used has a decisive effect on its distribution.

Changing the Péclet number form 0 to 100 slows down diffusion driven by concentration gradients and convection caused by the deformation becomes dominant.

Comparing the breakup process with (Fig. 3.120) and without (Fig. 3.121) surfactants in a breakup process due to Rayleigh distortions confirms that size and number of drops and satellite drops remain unaltered, but the surfactant distribution is striking: surfactant being convected to the end of the filament, without time for diffusion backwards, changing the drop properties.

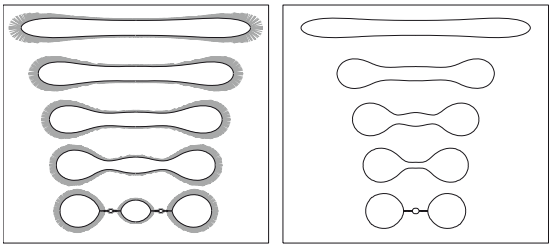

Figure 3.119: As Fig. 3.117, now with higher molecular weight soap ($\beta = 0.5$, Pe = 100). In daughter drops in centre: $\sigma = 1.62\,\sigma_{ref}$, while for outer drops: $\sigma = 1.20\,\sigma_{ref}$ [91]

5.5 Experimental Study of a Two-Dimensional, Nonstationary Flow

The journal bearing flow has been intensively studied by several authors (see, *e.g.*, Chaiken, *et al.* [15]; Ottino, *et al.* [2]). A viscous fluid is sheared between two eccentric and periodically rotating cylinders. Colored tracers permit visualization of the periodic stretching followed by folding up of flow regions, which is characteristic of chaotic motions. Experiments of the same kind have been carried out in our laboratory, but we have focused our attention on the reversibility of mixing.

A transparent Couette device with varying eccentricity and two independent and precise motors for the inner and outer cylinders was constructed. The respective diameters are 40 and 80 mm. A computer permits precise control of both the velocity and the position of the two cylinders. A glycerol fluid was used. The tracer obtained by centrifuging solid fluorescent particles with glycerol was injected with a syringe into the glycerol fluid at a distance approximately equal between the bottom and the free surface.

In one experiment, the inner cylinder is well centered, a drop of colored glycerol fluid is injected in the gap, and the outer cylinder is rotated five turns at a velocity of 5 rpm. The initial drop is sheared and changed into a ring, whose thickness is equal to the transverse dimension of the drop. The outer cylinder is then rotated in the opposite direction for the same time and at the same velocity. As expected, the drop is quite exactly reconstituted (see Fig. 5.14), demonstrating the low diffusion of the tracer.

In a second experiment, the inner cylinder is 10 mm off-center, a drop is injected in the gap, and the inner cylinder is rotated 10 turns at a velocity of 10 rpm. Depending on the initial location of the drop, different behaviors may be observed. In Fig. 5.15, the drop was initially located in the recirculation region. During the movement of the inner cylinder, it turns slowly, with a very low deformation level, within the recirculation (only 2.5 turns for 10 turns of the outer cylinder). When the cylinder is rotated in the opposite direction for the same period of time, the drop is only partially reconstituted. Different behaviors are observed if the drop is initially located near the inner cylinder, or near the outer cylinder (out of the recirculation), or on the saddle between the recirculation and the direct flow regions, but, in any case, the drop tends to be partially or totally reconstituted when the deformation is reversed. The second experiment points out that mixing may be better or worse depending on the initial location of the neighboring points.

In a third experiment, the inner cylinder is 10 mm off-center, after shearing several colored drops in a centered position (Fig. 5.16a). The inner and outer cylinders are rotated two turns alternatively (30 periods) in opposite directions at a velocity of 25 rpm. The initial drop is alternatively stretched and then folded up and characteristic "horseshoe" pictures may be observed (Fig. 5.16b, c). After 10 periods, the fluid seems to be homogeneous, which reflects a very good mixture (Fig. 5.16d). When reversing the flow protocol, the drop is not reconstituted and the entire gap – except for a narrow ring along the outer cylinder – remains colored.

Note that the dissipated energy is not very different in the last experiment compared to the preceding ones (or in a nonstationary experiment in which the inner cylinder is centered).

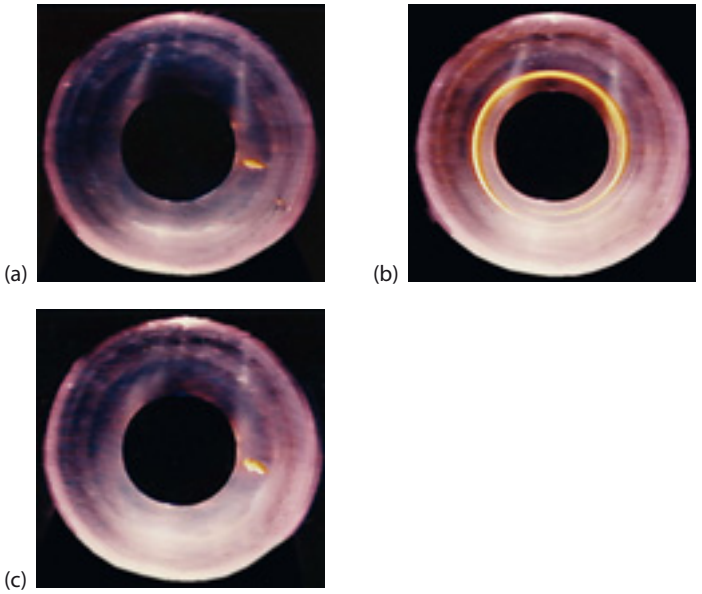

Figure 5.14: Couette flow: (a) initial drop location; (b) drop deformation after 5 turns at 5 rpm; (c) the drop is reconstituted after reverse deformation

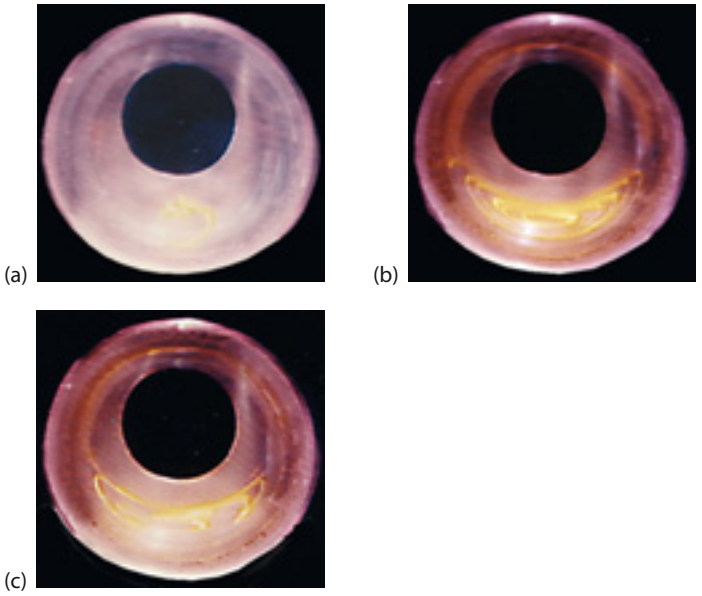

Figure 5.15: Eccentric Couette flow: (a) initial drop location; (b) drop deformation after 10 turns at 10 rpm; (c) after reverse deformation

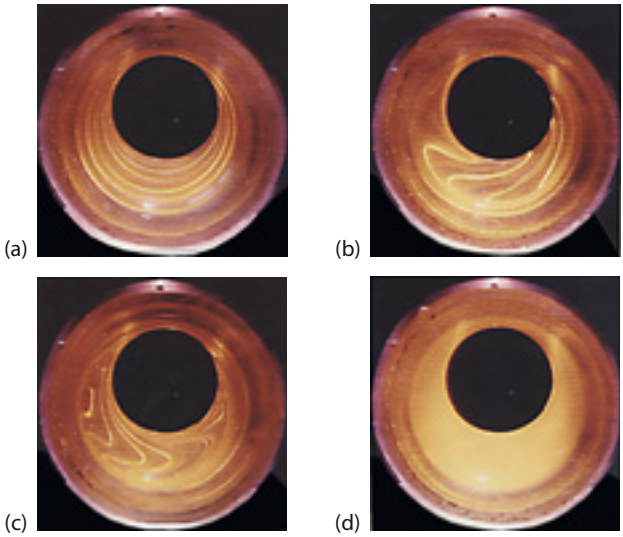

Figure 5.16: Eccentric Couette flow with alternative rotation of the inner and outer cylinders (25 rpm during 30 periods): (a) initial tracer distribution; (b) and (c) characteristic "horseshoe" images during the first period; (d) after 30 periods

This shows that the dissipated energy is not a suitable measure of mixing efficiency in the case of nonstationary two-dimensional flows.

From a physical point of view, this discrepancy may be explained by the existence of recirculating flows whose dimensions and locations are different when the inner and outer cylinders are rotating (Fig. 5.17) [15]. If we consider two neighboring points, which are located in the recirculation initially when the inner cylinder is rotating, we may find them suddenly separated when the inner cylinder is stopped and the outer cylinder is rotating, with one point located in the new recirculation and the other one in the direct flow. At each period, the same situation will be encountered but for different neighboring points, and mixing will be very efficient after a limited number of periods.

Several other two-dimensional nonsteady chaotic flows have been studied theoretically by Aref [16] and by Fortin *et al.* [17, 18].

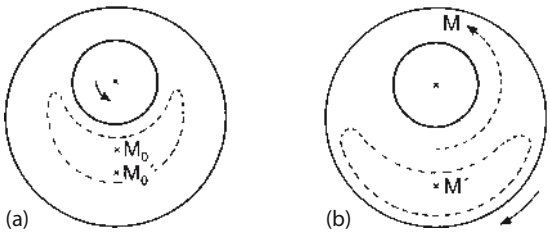

Figure 5.17: Eccentric Couette flow: schematic explanation of mixing efficiency; (a) inner rotating cylinder; (b) outer rotating cylinder

5.6 Application to Three-Dimensional Flow Configurations

5.6.1 Periodic Shearing Flow

Now, we examine a generalization of the two-dimensional flow of Section 5.4 (Fig. 5.18):

$$h(x, y) = a + b \sin^2(\pi\, x/1_x) \sin^2(\pi\, y/1_y) \tag{5.13}$$

A priori, this geometry seems to be far from a polymer processing geometry. However, the geometry of the dynamic mixer developed by the Rubber and Plastic Research Association (RAPRA) and installed at the end of a single-screw extruder is very close to this flow geometry (see Fig. 5.19).

Hydrodynamic lubrication approximations lead to the well-known Hele-Shaw equation for pressure:

$$\text{div}\,[h^3\ \text{grad}\ p] - 6\,\eta\, V\ \text{grad}\ h = 0 \tag{5.14}$$

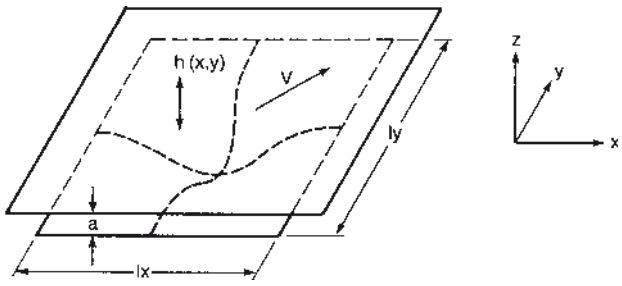

Figure 5.18: Three dimensional periodic flow

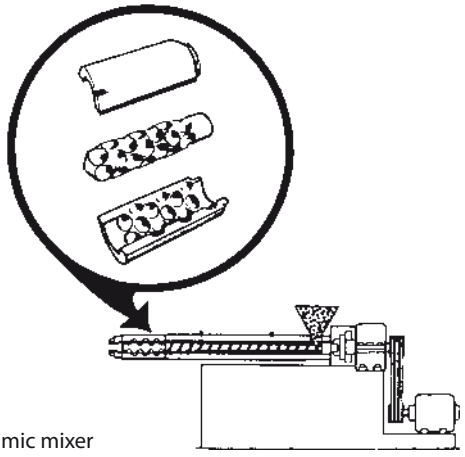

Figure 5.19: RAPRA dynamic mixer

ing pellets, or fragments, powder or other materials that the screws cannot wipe clean. This may limit the application of the system to thermally stable polymers or lower temperature operating conditions. If the windows are mounted in the melting zone, special care must be taken to avoid cracking or breakage due to high stress gradients in both axial and rotational directions. High-modulus materials, such as Polyamides, can generate very high forces over small areas in the melting zone. Special lighting should be used to minimize shadows and reflections that prevent high quality image capture. Linear light arrays mounted at an angle to the glass surface work well. Imaging hardware must be mounted so that extruder vibration does not move the camera relative to the window. The electronics must be protected from the barrel heat, steam and molten polymer with horizontal air jets and shielding. For safety, plastic shields may be used to protect operators and equipment from polymer leakage or window breakage.

Observations of the solid transport region using direct visualization methods have made significant contributions to the fundamental understanding impacting feed section and melting zone screw design [4]. Two solid transport paths were identified. At low degrees of fill, free flowing pellets slip on the screws and flow axially forward via positive displacement, in the nip on top and the belly of the channels on the bottom, forming three independent domains. As the degree of fill increases by raising the Q and N ratio, the nip area fills with pellets and the bottom of the channel fills to form one filled volume. Thus, two solid plugs are conveyed in the positive displacement mode. As the fill level is increased further, pellets begin to move in the figure-8 pattern around the channel. Finally, as pressure is generated at the beginning of the melting zone, frictional heating is observed, and a melt film may be formed as shown in Fig. 15.51. At very low screw speeds, partial melting was observed due to pellets being exposed to the heated barrels for long residence times. Figure 15.54 shows the fill effects on HDPE pellet flow in the solid conveying region of a 27 mm twin screw extruder.

15.2.3.7 Visualization of the Melting Zone by Direct Observation

The same methods used to visualize solid transport have been applied to observe the melting process in extruders. Gogos and his colleagues made extensive use of their Coperion W&P ZSK-30 mm twin screw mixing/melting element evaluator (TSMEE) fitted with a clam shell barrel to study the melting of pellets, powders, and polymer blends [9]. Figure 15.53 shows several examples of PP pellet and powder melting states after the machine was stopped, barrels cooled and clam shell opened. This work identified the basic stages of melting in the twin screw extruder and confirmed earlier phenomena described in batch mixer simulations. The effects of particle form (pellet and powder) on melting initiation and progression were quantified. The influence of a low melting point component in a polymer blend on melting was observed as well.

Geng and Zhu used contoured glass windows in a Leistritz 27 mm co-rotating and counter-rotating twin screw extruder for in-line observations [4]. The segregated solid bed and melt pool melting phenomenon, typical found in single screw extrusion, was not observed. Instead, pellets were dispersed in the melt phase ("islands in the sea") in the kneading zone as illustrated in Fig. 15.54. The direct visualization method has the added benefit of revealing

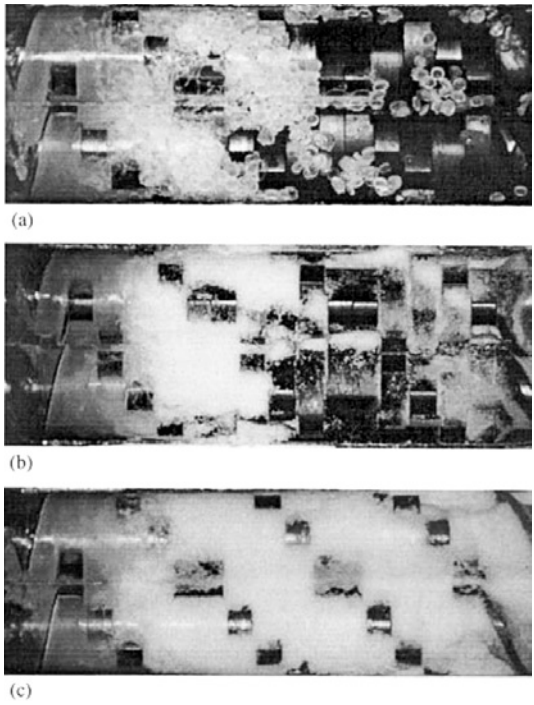

Figure 15.53: PP pellet and powder melting visualization using clam shell barrel running at 11.35 kg/hr and 250 rpm: a) pellets, b) powder, and c) powder with wax [9]

the dynamics of the melting phase transformation and material flows as the screws rotate. Sakai mounted a long glass window into the extruder barrel wall in the axial direction [4]. He was able to distinguish 3 different flow regimes: solid, melting and liquid regimes in both co-rotating and counter-rotating machines. He reported that the variation in the screw length required to complete melting depended on the screw design used.

Shih and his co-workers used visualization and torque/temperature measurements in a batch mixer to identify the sequential stages of melting of thermoplastics. They proposed that the same mechanisms occurred in the twin screw extruder [50, 51]. Gogos, Tadmor and their colleagues used the TSMEE clam shell system to study melting in the extruder [7–10]. They found clear evidence of the mixed-melting mode [1]. These experiments also showed that plastic deformation after solids compaction could consume most of the mechanical energy input to raise the temperature of the solids and initiate melting. Irreversible compressive plastic energy dissipation (PED) can effectively heat the interior of solid particles rapidly as opposed to the relatively slow conductive heat transfer rate from the barrel to the surface of the solids. Sakai [5, 27, 59], Potente [14–15] and others used the screw pull and carcass analysis technique and found evidence to support the existence of the dissipative mixed-melting mechanism. The twin screw melting sequence is clearly different from the well known single screw extrusion process and is summarized below:

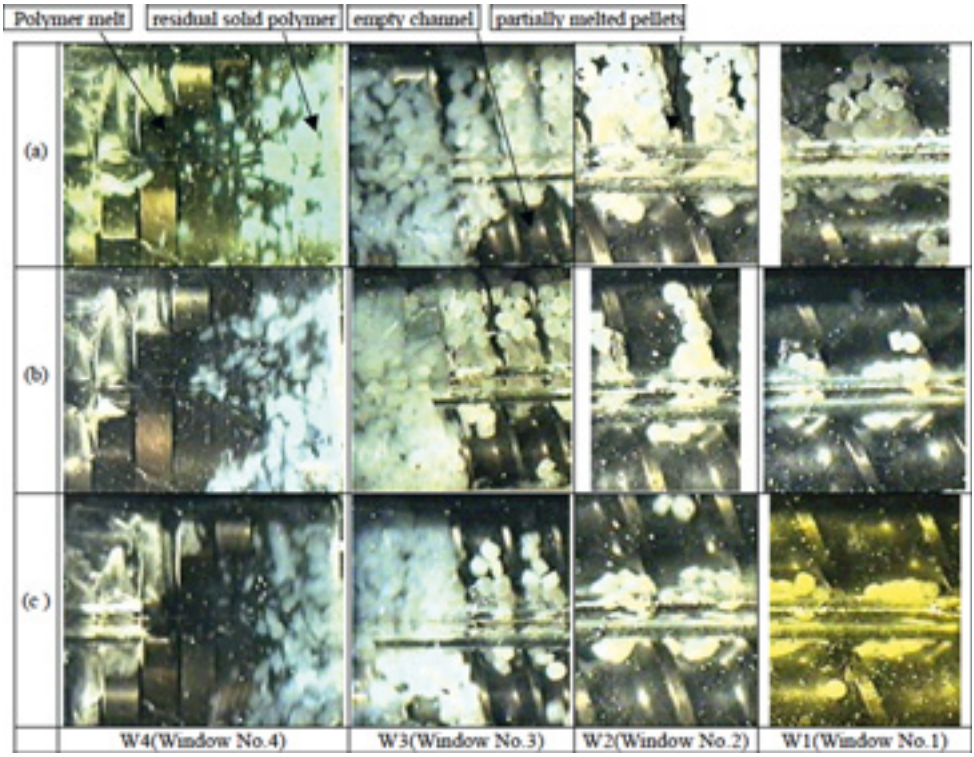

Figure 15.54: HDPE melting visualization using top-mounted glass window: 10 kg/hr with screw speeds of a) 50, b) 80, c) 110 RPM [4]

1. Solids conveying of free-flowing pellets or powders with heat transfer from the barrel, screw and hot air in the channel.
2. Solids compaction filling the channel due to the backfill from the restriction downstream at the end of the melting zone. At this "point of first fill", pressure increases and frictional heating of the pellet surfaces commence at the barrel wall and potentially between pellets as the solid bed realigns, or deforms, as it passes through the nip region. This is defined as frictional energy dissipation (FED).
3. Plastic deformation of the solid pellets (PED).
4. Formation of a melt phase that causes pellets to slip, reducing barrel friction and deformation.
5. Formation of a solids-rich melt suspension. Shear and extensional viscosities can be extremely high with solids content near a packing density. Significant heat is generated in the melt phase through viscous dissipation. Pellets continue to melt as heat flows from the melt phase to the solid surface. This is designated as the viscous energy dissipation (VED) mode with mix-melting.

6. As melting progresses, the viscous dissipation decreases with reduced solid concentration and the system behaves as a molten polymer with dispersed solids, a polymer-rich melt suspension (VED).
7. Liquid flow after melting is complete (VED).

Based on the visualization experiments, new insights into melting in twin screw extruders have impacted polymer compounding system development. Potente developed a predictive melting model based on first principles for solids transport, and dissipated mix-melting [14–15]. With the TMSEE observations, Gogos and Kim measured energy input and adiabatic temperature rise in molded polymer specimens subjected to compressive deformation using an analogous analytical test as shown in Fig. 15.55 [9]. Figure 15.56 shows compressive stress-strain and adiabatic temperature rise for polyethylene (PE), polypropylene (PP), polystyrene (PS) and (from other experiments) polyamide 6,6 (PA). An adiabatic temperature rise estimation method was developed by integrating the stress-strain curves to calculate the energy dissipation beyond the elastic region and determine the temperature increases from the material enthalpy change curves determined by DSC (see Fig. 15.5). The PA temperature rise shown in Fig. 15.56 was estimated using this approach. Gogos and his colleagues then developed a sequential dissipation model with heat source terms describing the bulk energy consumption in each melting step [7–10]:

$$\rho C_V \frac{DT}{Dt} = \underbrace{-\underline{\nabla} \cdot q}_{\substack{\text{Conductive} \\ \text{Heating}}} + \underbrace{\eta (\dot{\underline{\underline{\gamma}}} : \dot{\underline{\underline{\gamma}}})}_{\text{VED}} + \frac{d}{dt} \int_e^{de} \underbrace{\sigma_V}_{\text{PED}} \, d\varepsilon + \underbrace{n \, p \, F_n \, \Delta v}_{\text{FED}} + \dot{S} \tag{15.6}$$

This model has been used to estimate the mechanical and heat transfer energy input in a twin screw extruder required to melt different thermoplastics, predict the axial temperature profile and the length of the screw required to melt the polymer for a given screw configuration and operating condition. Equation (15.6) links the fundamental thermo-mechanical properties of a polymer to the twin screw process. This research has provided important insights into the melting process making an impact on industrial processes, including screw design and scale-up, and reducing energy consumption. The principles developed here can be linked to many batch mixer simulations and on-line monitoring examples described in this chapter.

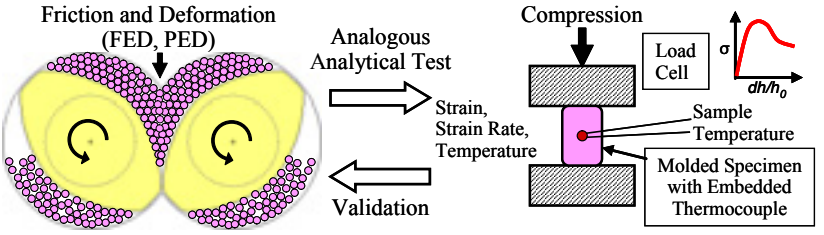

Figure 15.55: Apparatus to measure energy input and temperature rise in a polymer sample in compression to quantify energy dissipation during melting in a twin screw extruder [9]

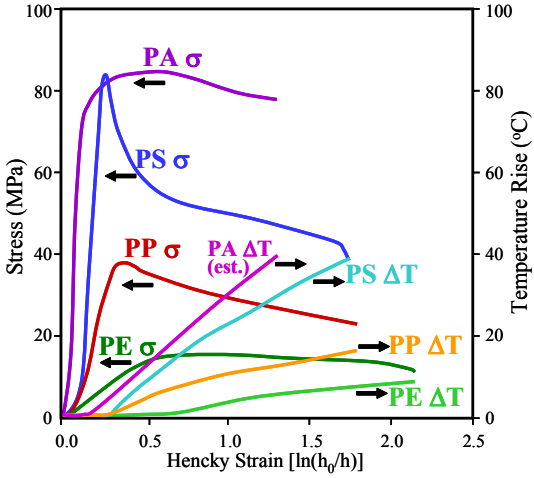

Figure 15.56: Compressive stress-strain curves and measured temperature rise for various thermoplastics [9]

For example, adiabatic temperature rise estimates measured in the compression test method or calculated from the stress-strain curves are consistent with energy input measurements from the mass pulse perturbation method [36–39].

15.2.3.8 Visualization and On-line Monitoring using Highly-Instrumented Extruders

McCullough at Dow Chemical did original on-line monitoring work by mounting a twin screw extruder barrel on a lathe to rotate the screws and measure axial and radial pressures using model fluids [11]. Christiano and Lindenfelzer at Davis-Standard extended this approach to a melt extrusion system [12]. They mounted the barrel assembly on a sliding mechanism. A spacer plate was added with eight pressure transducers located around the barrel periphery upstream of a mixing section. Pressures were recorded with a high-speed data acquisition system during a normal steady state melt extrusion. Data were recorded at a fixed axial location, the sliding mechanism was moved several millimeters downstream (in the flow direction) and then the measurements were recorded again. This process was repeated until dynamic pressure measurements were captured over the entire length of the mixing section. A two-dimensional pressure map was generated showing the high and low peaks and gradients as the screws rotated. Kneading blocks (KBs) with forward (designated RH), neutral (N) and reverse (LH) disk staggering were compared. Figure 15.57 shows axial and radial pressure maps for three KB's at different screw rotational angles. The data show that the disk staggering influence the localized pressure differences, gradients and average axial values. Different disk stagger angles and disk widths were also compared. From the pressure mapping, the effects of geometry were related to dispersive and distributive mixing performance. This pressure mapping technique can be considered a form of visualization making important

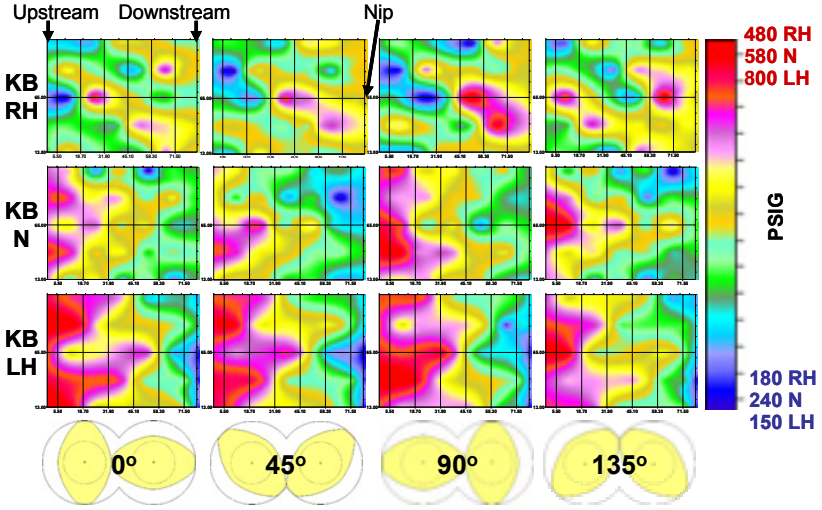

Figure 15.57: Dynamic axial and radial pressure mapping of forward pumping (RH), neutral (N) and reverse pumping (LH) KBs with screw rotation [12]

contributions to the understanding of the fluid mechanics, energy dissipation and mixing in melt extrusion processes. This approach can provide basic data to validate computer aided engineering (CAE) models and improve screw element design to maximize mixing efficiency while minimizing energy input and localized pressure differences.

Using this sliding barrel concept, Wetzel and his co-workers at DuPont extended Christiano's approach to study melting by adding glass windows for direct visualization, temperature, pressure and optical (RTD) probes on a Coperion W&P ZSK-40 mm co-rotating twin screw extruder as shown in Fig. 15.58 [13]. Using this highly-instrumented extruder, a high-speed data acquisition system was used to map melting zone pressures and temperatures by computing average and root mean squared (RMS) pressure and mean temperature axial profiles over a range of throughputs (Q) and screw speeds (N). The instrumentation section included a barrel fitted with a glass window on the top and a radial sensing plate as shown in Fig. 15.59. The radial sensing plate shown in Fig. 15.60 had eight "Dynisco" pressure ports that were angled so that the probes in the nip were flush with the inner wall and to accommodate barrel alignment pins and anchoring bolts.

The visualization system developed for these experiments illustrate important considerations in hardware selection, installation and use:

1. An imaging port must be designed for the visualization to withstand the processing temperatures and pressures. In this case, the glass window shown in Fig. 15.60 was shaped to fit the barrel contours in the nip region. It was heat treated to operate at temperatures up to 300 °C, and so that it would not crack during system heating and cooling. The window was placed in the barrel insert shown in Fig. 15.59. Gaskets were installed under the glass flange to provide enough clearance so that the rotating screws would not contact